Nano Research
2023, 16(7): 8919–8928

ISSN 1998-0124 CN 11-5974/O4
https://doi.org/10.1007/s12274-023-5598-x

Research Article

Nanostructured Ni-MoC_x: An efficient non-noble metal catalyst for the chemoselective hydrogenation of nitroaromatics

Yifei Zhang[1,2,§], Zhiwen Li[2,6,§], Jingjing Zhang[2], Liangliang Xu[3], Zhong-Kang Han[4] (✉), Alfons Baiker[5] (✉), and Gao Li[2,6] (✉)

[1] *Institute of Catalysis for Energy and Environment, College of Chemistry and Chemical Engineering, Shenyang Normal University, Shenyang 110034, China*
[2] *State Key Laboratory of Catalysis, Dalian Institute of Chemical Physics, Chinese Academy of Sciences, Dalian 116023, China*
[3] *Department of Chemical and Biomolecular Engineering, Korea Advanced Institute of Science and Technology (KAIST), Daejeon 34141, Republic of Korea*
[4] *School of Materials Science and Engineering, Zhejiang University, Hangzhou 310027, China*
[5] *Department of Chemistry and Applied Biosciences, Institute for Chemical and Bioengineering, ETH Zurich, Hönggerberg, HCl, Zurich CH-8093, Switzerland*
[6] *University of Chinese Academy of Sciences, Beijing 100049, China*
[§] *Yifei Zhang and Zhiwen Li contributed equally to this work.*

Received: 4 January 2023 / **Revised:** 18 February 2023 / **Accepted:** 19 February 2023

ABSTRACT

Catalysts for chemoselective hydrogenation are of vital importance for the synthesis of various important chemicals and intermediates. Herein we developed a simple method for preparing a highly efficient Ni-MoC_x nanocomposite catalyst via temperature-programmed carburization of a polyoxometalate precursor. X-ray diffraction (XRD), scanning transmission electron microscopy (STEM), X-ray photoelectron spectroscopy (XPS), and X-ray absorption spectroscopy (XAS) analyses indicate that the resulting mesoporous nanocomposite catalyst is made up of well-dispersed metallic nickel particles embedded in a MoC_x matrix. This catalyst exhibits high activity and selectivity (> 99%) in the hydrogenation of various substituted nitroaromatics to corresponding anilines. The high efficiency is attributed to the intimate contact of the constituents favoring electron transfer and hydrogen adsorption. Dihydrogen is physisorbed on the carbide support and dissociates on the nickel particles, as evidenced by Mo K-edge X-ray absorption near-edge structure (XANES) spectra, density functional theory (DFT), and hydrogen–deuterium exchange. The remarkable catalytic performance of the catalyst could be traced back to the synergistic interaction between the Ni particles and the carbide support. *In-situ* infrared spectroscopy and DFT simulations indicated that the adsorption/activation of the nitro group is favored compared to that of other substituents at the aromatic ring. In recyclability tests, the Ni-MoC_x nanocomposite showed no significant loss of catalytic performance in seven consecutive runs, indicating its robust nature.

KEYWORDS

Ni-MoC_x nanocomposite, carburization of polyoxometalate, hydrogenation, nitroaromatics, synergistic effect

1 Introduction

Functionalized anilines are key intermediates in the manufacture of various important chemicals, including pharmaceuticals, agrochemicals, dyes, and polymers [1–3]. Their production via chemoselective reduction of substituted nitroaromatics is a highly desirable yet rather challenging task, especially in the presence of other sensitive groups in the same substrate (e.g., halogen, alkenes, alkynes, and ketones) [4]. In recent decades, great advances in the metal-catalyzed selective hydrogenation of nitrostyrene have been made. A variety of promising supported noble metal catalysts including Pd [5–10], Au [11–14], and Pt [5, 15–17] have been developed, but it is still challenging to achieve high activity, chemoselectivity, and stability with non-noble metals. Poisoning or leaching of the active metal components can contaminate products and cause severe environmental issues detrimental to sustainable chemistry [18–20].

Compared to noble metal catalysts, 3d-non-noble metals including Ni [21–24], Fe [25–27], and Co [28, 29] are more desirable due to their low cost and widespread availability [30, 31]. Besides, the monometallic, also bi- and trimetallic catalysts, such as NiCu/C@SiO_2 and $LaCu_{0.67}Si_{1.3}$, were reported to exhibit very high activity [32, 33]. Among the non-noble metals, Ni-based catalysts are deemed to be efficient catalysts for selective hydrogenation. Either supported Ni nanoparticles or unsupported porous materials (such as Raney's Ni) are highly active for hydrogenation [34].

However, it remains still challenging to achieve both efficient catalytic turnover as well as absolute selectivity and stability in the hydrogenation of nitroaromatics. The high-temperature reduction for generating active metallic Ni species generally tends to lead to poor dispersion and thus reduced activity. Therefore, suitable supports are urgently needed to achieve stable highly-dispersed Ni

Address correspondence to Gao Li, gaoli@dicp.ac.cn; Zhong-Kang Han, hanzk@zju.edu.cn; Alfons Baiker, alfons.baiker@chem.ethz.ch

particles [35]. The selectivity of Ni catalysts has been constrained because most supported Ni catalysts are active for the reduction of the nitro group as well as for other unsaturated functional groups (e.g., C=C and C=O) existing in the same substrate. Various supports have been used for Ni-based catalysts [36–39], including γ-alumina, silica, carbon fibers, graphene/carbon nanotubes, and molybdenum disulfide, to overcome these difficulties. All these works indicate that the choice of support material is essential.

Recent advances indicate that transition-metal carbides could be explored as excellent supports for dispersing metals due to their noble metal-like electron configuration, which originates from d-band contraction in metal-carbon alloys. Moreover, the strong interaction between metals and carbides has been evidenced to be closely associated with the catalytic turnover and optimized selectivity over such carbide-supported metal catalysts [40, 41]. Among these transition-metal carbides, α-Mo_2C proved to be a promising material to support Ni. Its abundant surface species in an aqueous solution may result in stronger interactions with the dispersed metal and accelerate the reaction progress [42].

Inspired by these reports, we developed a simple method for preparing Ni-MoC_x nanocomposites by temperature-programmed carburization of a Ni-Mo-O polyoxometalate precursor (Scheme 1). The as-prepared catalyst consists of well-dispersed small Ni particles which are embedded in the carbide matrix. The intimate contact between Ni particles and the carbide support results in strong Ni-carbide interaction and remarkable performance and stability of this catalyst in the hydrogenation of various nitroaromatics to corresponding anilines.

2 Experimental

2.1 Materials

All chemicals, including the solvents, were commercially available as reagent grade and used as received without further purification. $Ni(NO_3)_2$ (98%), $(NH_3)_6Mo_7O_{24}$ (98%), nitrobenzene (99%), 4-nitrobenzaldehyde (97%), 3-nitrobenzaldehyde (98%), 1-bromo-3-nitrobenzene (98%), 1-nitro-4-vinylbenzene (98%), 1-chloro-3-nitrobenzene (98%), 3-nitrobenzonitrile (98%), 1,3-dimethyl-2-nitrobenzene (98%), 1,2-dimethyl-4-nitrobenzene (98%), and ethanol (99%) were purchased from Adamas-beta®. HZSM-5 with a SiO_2/Al_2O_3 molar ratio of 300 was purchased from Nankai University Catalyst Ltd. All the gases were purchased from the Dalian gas company. Ultrapure water was purified with a Barnstead Nanopure Di-water TM system. All glassware was thoroughly cleaned with aqua regia (37 wt.% HCl:HNO_3 = 3:1 by volume), rinsed with copious nano-pure water, and then dried in an oven before use.

2.2 Ni-MoC_x hybrid catalyst

The Ni-MoC_x nanocomposite was prepared via temperature-programmed carburization of a polyoxometalate precursor $(NH_4)_4Ni(OH)_6Mo_6O_{18}$ (Anderson cluster), which was synthesized according to the protocol described in Ref. [43]. Typically, 500 mg of the precursor was placed into a tube furnace under CH_4/H_2 atmosphere. The temperature was raised to 300 °C with a heating rate of 5 °C·min^{-1}, followed by heating to 500 °C with 2 °C·min^{-1} for 30 min, and finally to 600 °C with 1 °C·min^{-1} for 2 h. After this treatment, the as-prepared Ni/MoC_x nanocomposite was quickly cooled to room temperature and collected after passivation by exposing it to 1 vol.% oxygen balanced by Ar. The loading of Ni species determined by inductively coupled plasma-mass spectrometry (ICP-MS) amounted to 4.5 wt.%. The Ni-free MoC_x reference samples were obtained by carburization of $(NH_4)_6Mo_7O_{24}·4H_2O$ using the same procedure.

Ni@ZSM-5 catalyst. Typically, 16 mg $Ni(NO_3)_2·6H_2O$ was dissolved in 10 mL water, and 200 g Mes-HZSM-5 zeolite powder was added. After stirring overnight at room temperature, the solid was collected by centrifugation and then dried in air at 80 °C. Further, the sample was annealed at 550 °C for 4 h in air and then reduced in the presence of 100% hydrogen at 400 °C for 2 h [44].

2.3 Catalyst characterization

Powder X-ray diffraction (XRD) patterns of the samples were recorded on a D/Max-2500/PC diffractometer (Rigaku, Japan) with Cu Kα (λ = 0.154 nm) radiation operated at 40 kV and 200 mA in the range of 20° to 90° with a rate of 5 °·min^{-1}. The specific surface area was determined using nitrogen adsorption at 77 K and the Brunauer–Emmett–Teller (BET) method. Pore size distributions were derived from nitrogen desorption isotherms using the Barrett–Joyner–Halenda (BJH) method. The Ni content was analyzed using ICP-MS (NexION 300X, Perkin Elmer) by dissolving the Ni samples in boiling aqua regia (4 mL solution). Scanning transmission electron microscopy (STEM) images were recorded on an F200 microscopy operated at 300 kV. TEM (high-resolution TEM (HRTEM)) images were taken on a Philips Tecnai G2 F30 microscopy operating at 300 kV. The specimens were prepared by ultrasonically dispersing the sample into ethanol, depositing droplets of the suspensions onto a carbon-enhanced copper grid, and drying them in air. High-resolution X-ray photoelectron spectra (XPS) were measured using an ESCALAB MK-II spectrometer with an aluminum anode for Kα ($h\nu$ = 1484.6 eV) radiation. The equipment base pressure was 1.7 × 10^{-10} bar, and all samples were characterized at room temperature. Detailed spectra were recorded for the region of Ni 2p, O 1s, and Mo 3d photoelectrons with a 0.1 eV step. The analysis was performed using the XPSPEAK41 software, and charging effects were corrected by adjusting the binding energy (BE) of C 1s to 284.6 eV. The spectra were deconvoluted using the XPSPEAK program by curve-fitting with a mixed Gaussian–Lorentzian function. X-ray absorption spectroscopy (XAS) was conducted at the 4B9A beamline of the Beijing Synchrotron Radiation Facility (BSRF). The storage ring of BSRF was operated at 2.5 GeV with a stable current of 400 mA. Using a Si (111) double-crystal monochromator, the data were collected in fluorescence mode with a Lytle detector. All spectra were collected at ambient conditions. For H_2-temperature-programmed desorption (H_2-

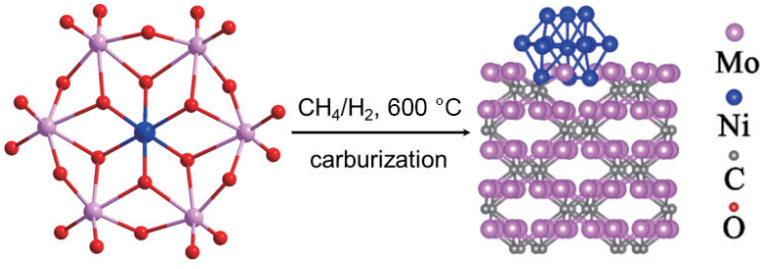

Scheme 1 Preparation procedure of Ni-MoC_x nanocomposite by temperature-programmed carburization of a polyoxometalate precursor $(NH_4)_4Ni(OH)_6Mo_6O_{18}$.

TPD) analyses, the catalyst was packed into a quartz reactor and heated under a He flow at 300 °C for 2 h. Then the reactor was cooled to 0 °C under flowing He (40 mL·min^{-1}). After saturation of the sample by exposing it to 10 vol.% H_2 at 0 °C for 0.5 h, the excess H_2 was removed by exposing the sample to flowing He until no H_2 could be detected anymore in the effluent. The desorption was initiated by ramping the temperature to 600 °C at a heating rate of 20 °C·min^{-1}. The desorption of hydrogen species was monitored by gas chromatography-mass spectrometry (GC-MS) at m/z = 2. X-ray absorption near-edge structure (XANES) and extended X-ray absorption fine structure (EXAFS) spectra at the Ni K-edge were accomplished on the 1W1B beamline of Beijing Synchrotron Radiation Facility, and the *in-situ* XANES spectra at the Mo K-edge on the BL14W1 beamline of Shanghai Synchrotron Radiation Facility.

2.4 Catalytic tests

The catalytic tests were conducted in a 10 mL stirred batch reactor at 140 °C and 20 bar H_2 for 4 h. Typically, 2 mL H_2O, 50 mg substrate, and 5 mg catalyst were used at a stirring rate of 600 rpm. After the reaction, the catalyst was collected by filtration, washed with water and ethanol, and dried at 100 °C overnight. The same procedure was used for testing the recyclability of the catalyst. The final products were extracted by ethyl acetate from the reaction solution and further separated by centrifugation. The supernatant was analyzed using a GC/MS 7890B-5977A equipped with a capillary column HP-5MS (length 30 m). Helium was used as carrier gas and p-xylene as an internal reference. The conversion of nitroaromatics ($XArNO_2$) and the selectivity to corresponding anilines ($SArNH_2$) were determined by GC-MS using an internal standard method, and calculated as

$$X_{ArNO_2} = \frac{C_0 - C_1}{C_0} \times 100\% \quad (1)$$

$$S_{ArNH_2} = \frac{C_{ArNH_2}}{C_0 - C_1} \times 100\% \quad (2)$$

$$TOF = \frac{mol_{reacted\ PhNO_2}}{mol_{nickel} \times time} \quad (3)$$

where, C_0, C_1, and C_{ArNH_2} represent the initial concentration of nitroaromatics, and concentrations of nitroaromatics and anilines after the catalytic hydrogenations, respectively. The average turnover frequency (TOF) was determined from initial rate data and the whole nickel content of the catalyst. Thus, it represented a conservative estimate.

2.5 Fourier-transform infrared (FTIR) spectroscopy

Typically, 10 mg of adsorbates (nitrobenzene, benzaldehyde, or 4-nitrobenzaldehyde) and 15 mg of Ni-MoC_x samples were mixed in a 5 mL methanol solution. After static storing in a refrigerator for 24 h, the black solids were collected and washed with methanol to remove the excess adsorbates and then dried at 60 °C for 2 h. The samples were further analyzed by infrared (IR) at different temperatures. The system was swept by flowing He (40 mL·min^{-1}) for 2 h. Spectra were recorded at 4 cm^{-1} spectral resolution and 60 kHz of scanning velocity at each temperature from 60 to 180 °C. The corresponding samples treated at 300 °C were used as references.

2.6 Density functional theory (DFT) calculation

The calculations were conducted within the Viena *ab initio* simulation package (VASP) [45, 46], and the structure optimization was based on DFT. The modeling of exchange-correlation energy was performed with the implemented generalized gradient approximation (GGA), proposed by Perdew–Burke–Ernzerhof (PBE) [47]. The valence electronic states were expanded with the plane waves, and the core–valence interactions were described using the projector augmented wave (PAW) approach [48], with the corresponding cutoff kinetic energies set to 400 eV. The Brillouin zone was set with a Gamma-centered k-point grid of 1 × 1 × 1 [49]. The structures were first relaxed with the implemented conjugate-gradient algorithm, until the convergence tolerance of Hellmann–Feynman forces and energy on each atom was less than 0.05 eV·Å^{-1} and 10^{-4} eV·atom^{-1}, respectively. Moreover, due to the periodic boundary conditions (PBC), there exist non-negligible interactions among periodical images; to reasonably overcome this, a separate vacuum layer, with a thickness of 20 Å along the z-direction, was applied. In addition, for all the calculations, spin polarization and dipole correction were considered.

3 Results and discussion

3.1 Textural and structural properties of Ni-MoC_x

The textural and structural properties of the Ni-MoC_x catalyst prepared by carburization of the polyoxometalate precursor were characterized using powder XRD, STEM/TEM, XPS, XAS, H_2-TPD, hydrogen–deuterium exchange experiments, nitrogen adsorption–desorption, and ICP-MS, as described in the Experimental section. The XRD patterns, presented in Fig. 1(a), indicate that the crystalline phase of molybdenum carbide in Ni-MoC_x was mainly comprised of Mo_2C (JCPDS #35-0787) [50]. In addition, XRD reflections at ~ 44.3° and ~ 51.5° were observed, corresponding to Ni (111) and Ni (200) reflections of metallic nickel particles (JCPDS #04-0850). Note that no other nickel species (e.g., NiO, Ni_2O_3, and NiC_x) were observed, confirming that the Ni-MoC_x nanocomposite was mainly composed of metallic Ni nanoparticles and the Mo_2C support. The Ni loading of the Ni-MoC_x catalyst determined by ICP-MS was 4.5 wt.%. The BET surface area amounted to 110 m^2·g^{-1} and the nitrogen adsorption–desorption isotherms (Fig. 1(b)) exhibited a type-IV isotherm with H3 hysteresis loop. The pore size distribution (inset of Fig. 1(b)) determined using the BJH method indicated a most frequent pore size of ~ 2.1 nm.

STEM with energy-dispersive X-ray (EDX) elemental mapping was applied to analyze the distribution of the Ni nanoparticles and the constituents of the MoC_x support, as shown in Fig. 2. In the corresponding HRTEM image (Fig. 2(b)), the lattice fringes associated with Mo_2C (100) and Ni (111) facets are discernible and the average size of Ni nanoparticles is about 45 nm. A histogram of the Ni particle sizes is presented in Fig. S1 in the Electronic Supplementary Material (ESM). The EDX elemental mapping indicates a random distribution of the Ni particles and MoC_x (Fig. 2(c)). The nickel nanoparticles were in intimate contact with the MoC_x support, allowing electron transfer between these components, which seems to be at the origin of the enhanced performance in the hydrogenation of nitroaromatics due to a synergistic effect (*vide infra*).

3.2 Surface properties

The surface properties of Ni/MoC_x nanocomposite were studied using XPS, XAS, H_2-TPD, and H_2-D_2 exchange measurements. XPS was used to investigate the chemical composition and valence state of the transition metals in the Ni-MoC_x nanocomposite. Mo 3d XPS spectra of Ni-MoC_x are presented in Fig. 3(a). Three characteristic chemical states (+2, +4, and +6) of Mo are discernible, which can be ascribed to the partial surface oxidation

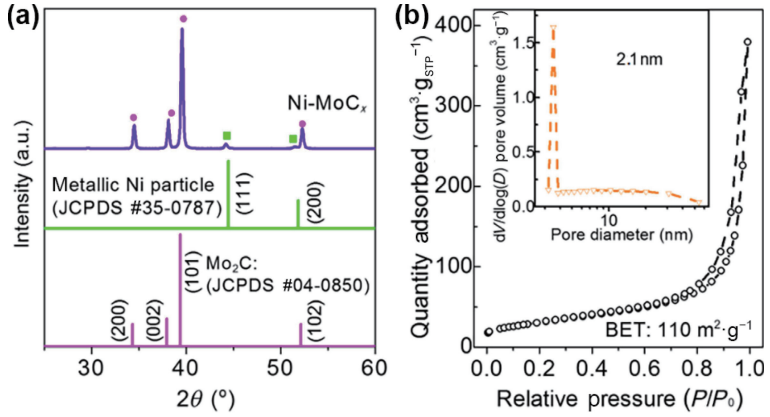

Figure 1 (a) XRD patterns and (b) N_2-adsorption–desorption isotherms of Ni-MoC_x nanocomposite. The reflections marked in (a) with pink balls and green squares are assigned to the MoC_x support and metallic Ni^0 particles, respectively. The inset in (b) shows the corresponding pore size distributions.

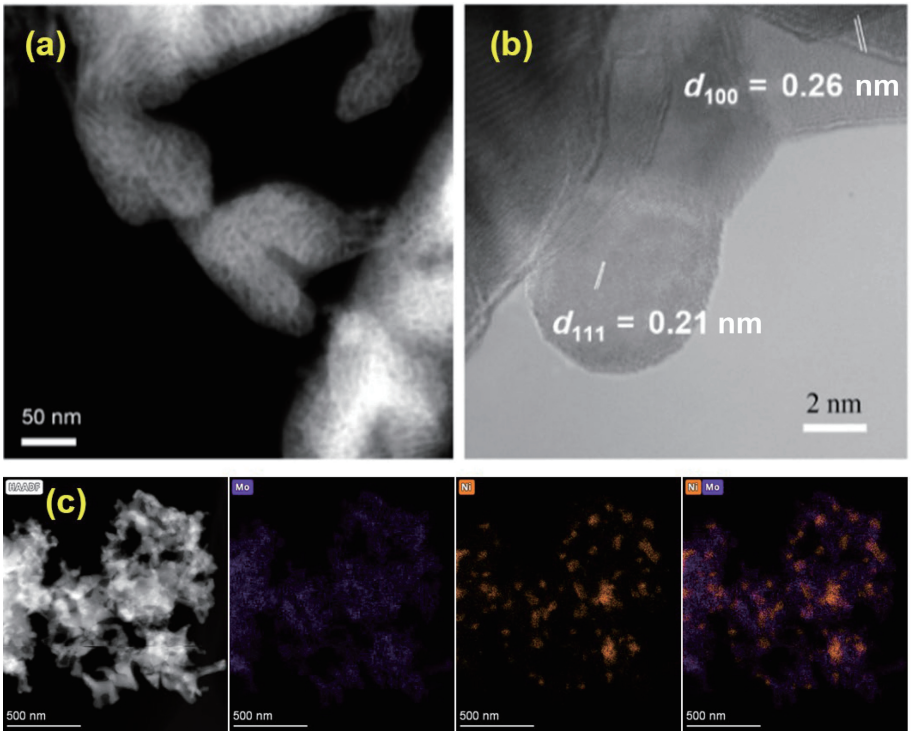

Figure 2 (a) STEM and (b) HRTEM images of the as-synthesized Ni-MoC_x catalyst. (c) TEM image of selected area and corresponding EDX mappings of Mo (purple) and Ni (orange) elements in Ni-MoC_x.

of MoC_x when exposed to ambient conditions [51, 52]. The binding energies at 228.4 and 231.6 eV belong to the Mo $3d_{5/2}$ and Mo $3d_{3/2}$ of Mo^{2+} in Ni-MoC_x, respectively. The negatively shifted peaks indicate a lower valence of Mo species [53]. As shown in Fig. 3(b), three peaks associated with Ni $2p_{3/2}$ appeared together with corresponding shake-up satellites. The binding energy peaks at 852.8 and 856.1 eV belong to metallic Ni^0 species and Ni(II) species, assigned to Ni–Ni and Ni–O bonding [54, 55]. The appearance of Ni–O bonding was caused by the exposure of the Ni-MoC_x samples to air and partial oxidation. The XPS peak at 859.4 eV hints a strong interaction of the nickel particles and MoC_x support, in which nickel contributes electrons to MoC_x due to their similar d-band state [56, 57]. Generally, the interatomic charge transfer and the subsequent modification of the surface electronic configuration have an important impact on the catalytic performance of Ni-MoC_x [58].

The coordination environment and electronic state of nickel in the Ni-MoC_x sample were confirmed using XANES and EXAFS with a standard Ni foil and a NiO oxide reference sample. As depicted in Fig. 3(c) and Fig. S3 in the ESM, the absorption Ni K-edge location of Ni-MoC_x showed similar features as the Ni foil, indicating the predominant existence of Ni–Ni bonding. The Fourier transformed (FT)-EXAFS spectra in Fig. 3(d) disclosed a bond distance (R) peak at 2.18 Å, corresponding to Ni–Ni bonding, corroborating the presence of metallic Ni^0 species [59, 60]. Notably, a very weak characteristic Ni–O peak was observed typically at 1.57 Å (Fig. 3(d)) [61], corroborating the presence of some NiO. These findings are well in line with the XPS analyses and suggest the formation of metallic Ni nanoparticles.

Furthermore, we also monitored *in-situ* the Mo K-edge XANES spectra of the Ni-MoC_x catalyst in the presence of a H_2 flow in the temperature range of 20 to 300 °C. Interestingly, the absorption Mo K-edge locations were perfectly overlapped, as delineated in Fig. 3(e), which indicates that the hydrogen molecules are dissociated (activated) on the metallic Ni particles rather than on the MoC_x support.

To investigate the ability of the Ni-MoC_x composite to activate hydrogen, we applied H_2-TPD and hydrogen–deuterium exchange mass spectrometry (Fig. 4), which are powerful tools to shed light on the catalyst's ability to dissociate H_2/D_2. The H_2-TPD profile (Fig. 4(a)) is dominated by a strong peak at 95.7 °C, which is assigned to the desorption of adsorbed [H] species over the Ni-

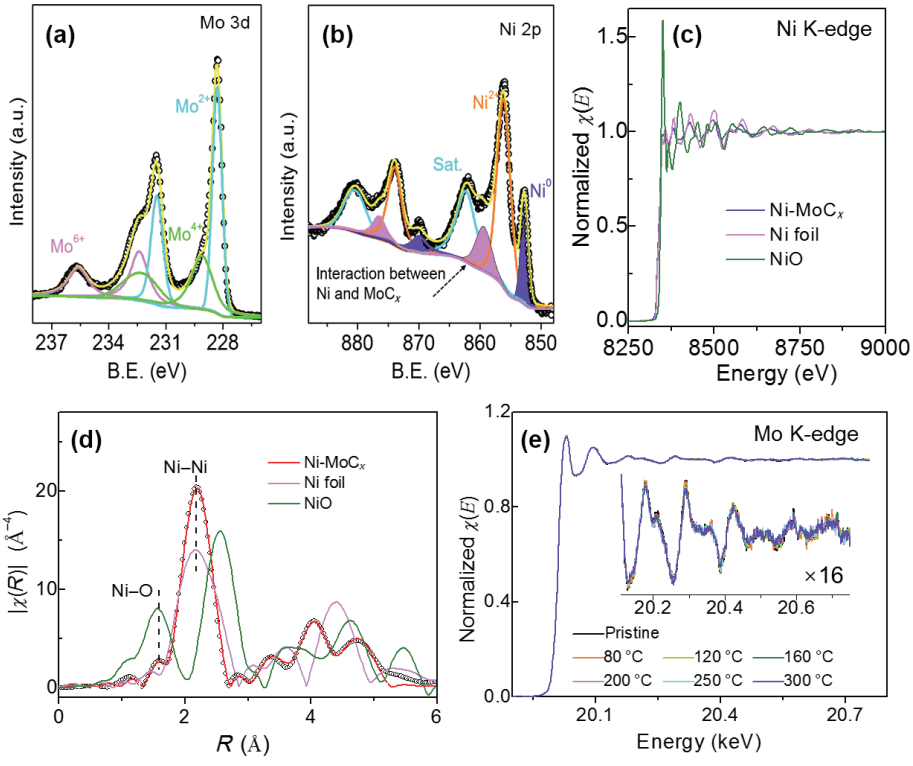

Figure 3 XPS and XAS analyses: (a) Mo 3d and (b) Ni 2p. The Ni 2p XPS peaks highlighted in purple and pink are the BE peaks for metallic Ni^0 species and interaction between Ni and MoC_x, respectively. (c) Normalized Ni K-edge XANES and (d) FT-EXAFS spectra of Ni-MoC_x and standard samples of Ni foil and NiO oxide. (e) *In-situ* monitoring Mo K-edge XANES spectra of Ni-MoC_x catalysts in the presence of H_2 flow at the temperatures of 20 to 300 °C; inset: zoom-in of the XANES spectra.

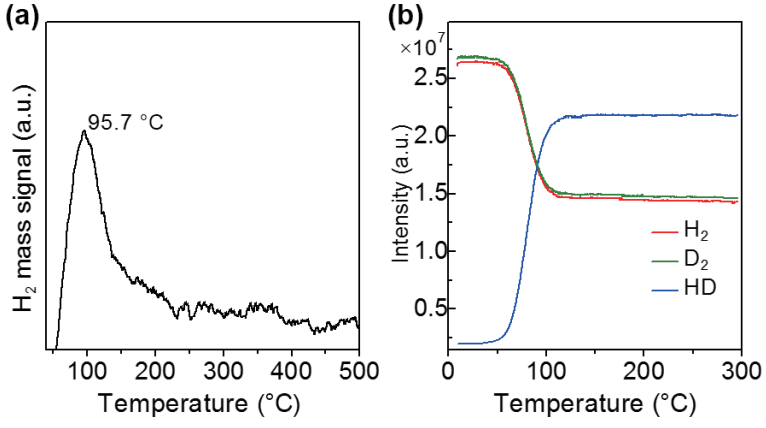

Figure 4 (a) H_2-TPD and (b) hydrogen–deuterium exchange ($H_2 + D_2 \leftrightarrow 2HD$) over Ni-$MoC_x$ catalyst.

MoC_x catalyst [61]. In the hydrogen–deuterium exchange experiments presented in Fig. 4(b), the initial exchange ($H_2 + D_2 \rightarrow$ 2HD) begins at ca. 50 °C and the equilibrium is attained at ca. 120 °C. Note the almost similar consumption of hydrogen and deuterium, indicating an equivalent reaction of H_2 and D_2. These results reveal that the Ni-MoC_x composite has a strong ability for dissociating hydrogen molecules at relatively low temperatures (e.g., > 50 °C), which indicates that the Ni-MoC_x composite is a promising candidate for hydrogenation catalysis.

3.3 Chemoselective hydrogenation of nitroaromatics

The hydrogenation of nitrobenzene to aminobenzene was chosen to evaluate the catalytic behavior of Ni-MoC_x composites. Note that the plain MoC_x support was inactive for the hydrogenation under the reaction conditions used (i.e., 2 MPa of H_2, at 140 °C). However, the Ni-MoC_x nanocomposite showed promising activity, with 93% conversion in 4 h at 100% selectivity to aminobenzene. The TOF, derived from initial rate data, reached 2390 $mol_{PhNO_2} \cdot mol_{Ni}^{-1} \cdot h^{-1}$ (Fig. S4 in the ESM), which is among the higher ones achieved with non-noble mono-metallic catalysts (Table S1 in the ESM). The Ni@ZSM-5 reference catalyst used under the same conditions showed much lower activity (Table S2 in the ESM), which indicates the high suitability of the carbide support and the important role of the intimate contact between the Ni particles and the MoC_x support. Next, we expanded the scope of substrates to nitrobenzene derivatives to investigate the influence of aromatic ring substitution. The substitution with electron-donating groups (e.g., methyl ($-CH_3$), vinyl ($-CH=CH_2$), and halides (Cl and Br)) significantly influenced the reaction as the conversion of the nitro group with these substituents decreased to 57%–85% (Table 1). The Ni-MoC_x catalyst exhibited excellent chemoselectivity (> 99%) toward the $-NO_2$ hydrogenation. Note that –CHO substitution at meta-position increased the conversion to 99% (entry 3), possibly due to the intramolecular interactions between the closely-located carbonyl and nitro groups (*vide infra*). Further, the Ni-MoC_x catalyst also showed remarkable catalytic performance (47% conversion) for derivatives with sterically hindering groups (e.g., 2,6-dimethylnitrobenzene, entry 9 in

Table 1 Screening of substrates with nitro groups over the Ni-MoC_x catalyst. Reaction conditions: 5 mg catalysts, 50 mg substrates, 2 mL H_2O, 2 MPa H_2, at 140 °C for 4 h or for 10 h[a]

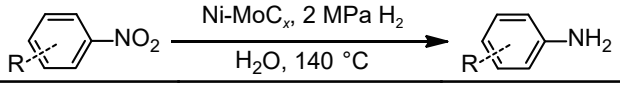

Entry	Substrate	Product	X_{ArNO_2} (%)	S_{ArNH_2} (%)
1	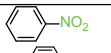	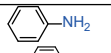	93	100
2	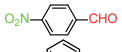	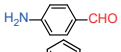	56 (100)[a]	> 99
3	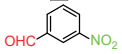	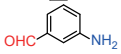	99	> 99
4	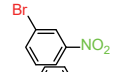	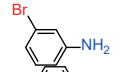	72	> 99
5	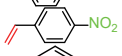	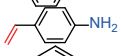	62	> 99
6	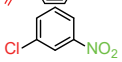	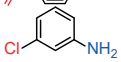	85	> 99
7	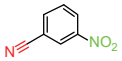	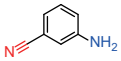	56	> 99
8	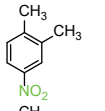	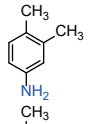	65	100
9	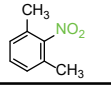	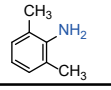	47	100

Table 1). Note that the chemoselectivity of $-NO_2$ hydrogenation was still > 99% when the 4-nitrobenzaldehyde conversion reached up to 100% at 10 h reaction time (entry 2 (bracket) in Table 1). This is further substantiated by comparing the catalytic performance of Ni-MoC_x with the Ni@ZSM-5 catalyst [44] under identical conditions (Table S2 in the ESM).

These results show that the Ni-MoC_x catalyst favored the hydrogenation of the nitro group compared to the other sensitive groups (e.g., methyl, vinyl, cyano, formyl, and halides). To confirm this result, control experiments were conducted using a mixture of nitrobenzene and other substrates (styrene or benzaldehyde). Note that styrene was hardly converted even at a prolonged reaction period, while the nitrobenzene was completely converted to aminobenzene (entry 1 in Table S3 in the ESM). In addition, the selectivity of the hydrogenation to benzaldehyde also strongly decreased when adding nitrobenzene into the reaction system, and the formation of the Schiff base compounds occurred instead of benzyl alcohol (entry 2 in Table S3 in the ESM), which demonstrates that the –CHO reacted with aniline when the $-NO_2$ group was completely converted [62]. Previously, Corma and coworkers showed that on an Au/TiO_2 catalyst both the nitro and vinyl groups can adsorb, while the nitro group is favored compared to the vinyl group [11]. Tan et al. also reported that an Au_{25}/ZnAl-HT-300 catalyst is virtually inert for the vinyl group and is only active for transforming the nitro group [63]. Interestingly, on the Ni-MoC_x catalyst, the nitro group and the formyl group were not competitively chemisorbed, as corroborated by *in-situ* FTIR experiments (*vide infra*) (Figs. S6–S8 in the ESM). Instead, only the nitro group was selectively activated over the Ni-MoC_x composite while the other groups were not. This led to the high chemoselectivity for hydrogenation of the nitro group achieved with this catalyst. Further, we examined the catalytic performance of the reused Ni-MoC_x in the hydrogenation of 4-nitrobenzaldehyde to assess its recyclability. Using the recycled catalyst, reactions were run with fresh reactants under the same conditions. As shown in Fig. S5 in the ESM, conversion and selectivity were maintained during a test with seven cycles, confirming the recyclability of the nanocomposite catalyst and the high chemoselectivity (> 98%) of the $-NO_2$ reduction. No appreciable loss of catalytic activity and selectivity was observed in the recyclability test, which confirmed the robust nature of the Ni-MoC_x nanocomposite as an efficient catalyst for hydrogenation.

3.4 FTIR study of substrate adsorption

The adsorption behavior of different substrates on the Ni-MoC_x catalyst was examined by *in-situ* FTIR. The Ni-MoC_x was placed in a solution containing the specific substrate (nitrobenzene, benzaldehyde, or nitrobenzaldehyde) at 4 °C for 24 h, and then monitored by FTIR at different temperatures from 60 to 160 °C. Details of the experimental procedure are described in the Experimental section. As shown in Fig. 5(a) and Fig. S6 in the ESM, the intensity of the band indicative of the stretching vibrations of the nitro group at ~ 1558 and 1398 cm^{-1} [64] slightly decreased due to partial desorption of nitrobenzene at higher temperatures. However, chemisorbed nitrobenzene remained on the Ni-MoC_x surface even at 160 °C.

In contrast, the stretching vibration of the carbonyl group (1698 cm^{-1}) [65] of benzaldehyde adsorbed on Ni-MoC_x was very weak (Fig. 5(b) and Fig. S7 in the ESM) and nearly disappeared at 100 °C, indicating that virtually all benzaldehyde was removed. The comparative IR study substantiates that the nitro group strongly binds to the Ni-MoC_x surface, whereas the carbonyl group of the aldehyde only binds very weakly. This different adsorption behavior is proposed to be at the origin of the high chemoselectivity toward the nitroaromatics reduction to amines. Nitrobenzaldehyde is also strongly adsorbed on the Ni-MoC_x nanocomposite, further substantiating the different adsorption behaviors of nitrobenzene and benzaldehyde (Fig. S8 in the ESM).

3.5 Tentative reaction mechanism

First-principles calculations were used to gain deeper insight into the mechanism of the hydrogenation of 4-nitrobenzaldehyde to 4-aminobenzaldehyde on the Ni-MoC_x catalyst and to reveal the reason for its excellent performance. Figures 6(a) and 6(b) show that the 3d orbitals of Ni resonate with the 4d orbitals of Mo near the Fermi energy in the Ni-Mo_2C composite, indicating the hybridization between Ni-Mo d orbitals. Figure 6(c) depicts the

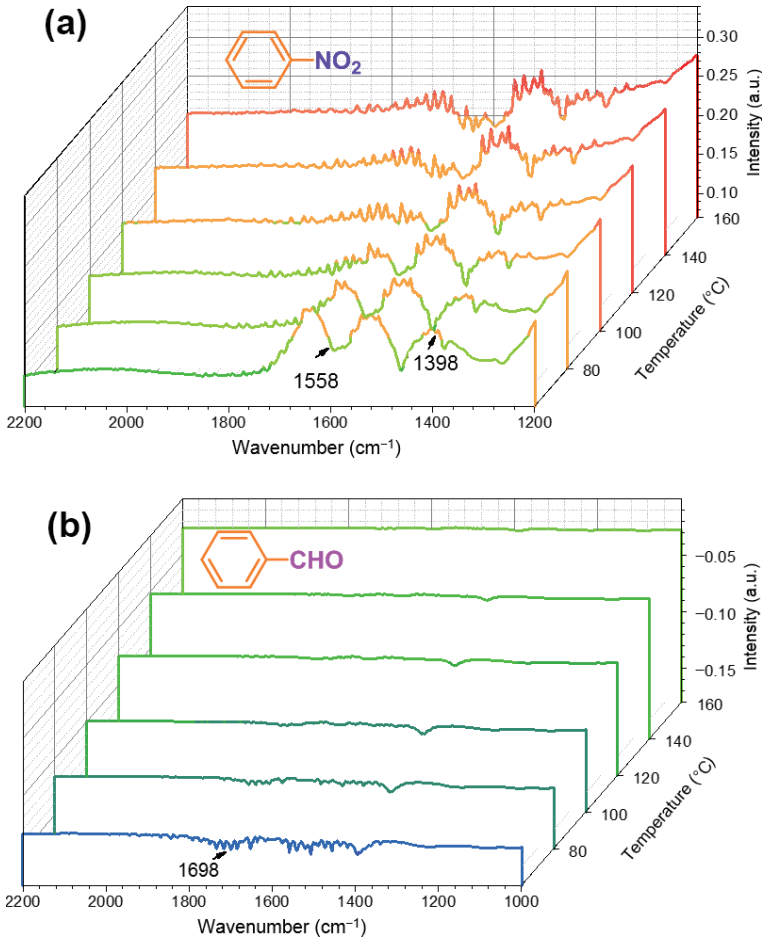

Figure 5 Temperature-dependent desorption of adsorbed: (a) nitrobenzene and (b) benzaldehyde from Ni-MoC_x monitored by FTIR. Conditions are described in the Experimental section.

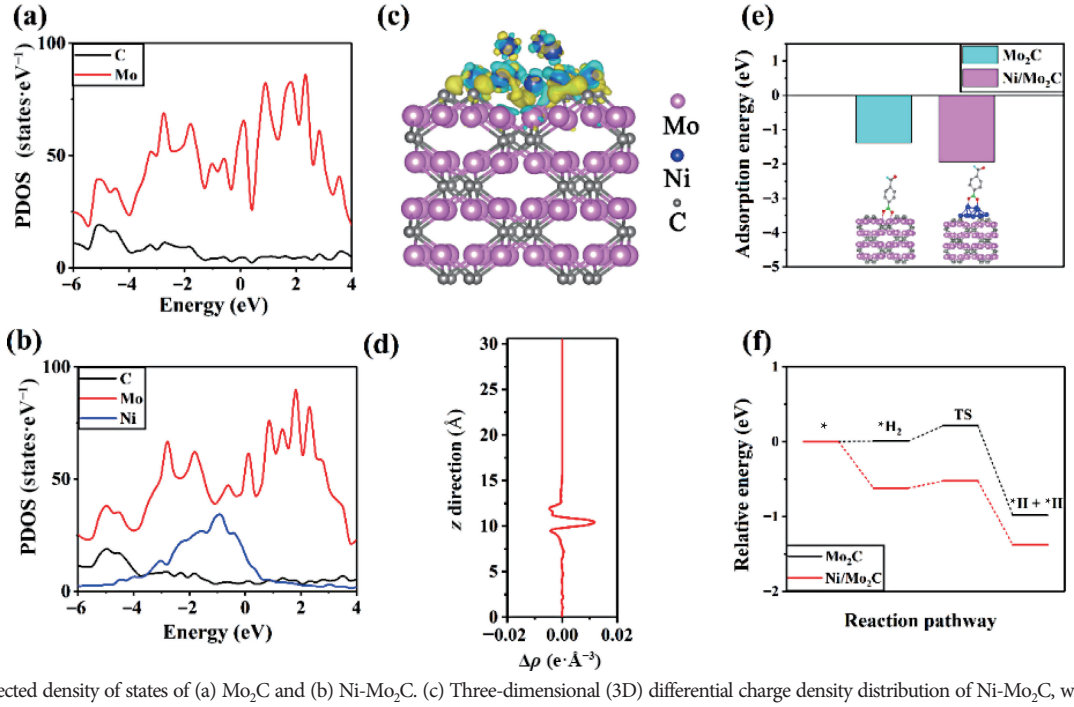

Figure 6 Projected density of states of (a) Mo_2C and (b) Ni-Mo_2C. (c) Three-dimensional (3D) differential charge density distribution of Ni-Mo_2C, where the yellow and cyan area indicate electron enrichment and loss, respectively. (d) The *xy*-plane-averaged differential charge density. (e) The adsorption energy of 4-nitrobenzaldehyde ($C_7H_5NO_2$) on pure Mo_2C and Ni-Mo_2C systems. (f) The adsorption and dissociation of hydrogen molecules on pure Mo_2C and Ni-Mo_2C systems.

differential charge density distribution between the Ni particle and the Mo_2C support, in which there is a large amount of charge transferred between the Ni particle and Mo_2C. Figure 6(d) displays the *xy*-plane-averaged differential charge density of the Ni-Mo_2C system along the (001) direction, indicating electrons transferred from Ni particle to Mo_2C. Bader charge analyses (Table S4 in the ESM) further confirmed that the Ni particle is positively charged with around 1.59 e. All these results are consistent with the experimental observations.

We further investigated the activation processes of the reactants

on both the clean Mo_2C and Ni-Mo_2C systems. As shown in Fig. 6(e), the adsorption of 4-nitrobenzaldehyde on Ni-Mo_2C is much stronger than on Mo_2C, which facilitates the following hydrogenation reaction. To locate the most stable adsorption configuration of 4-nitrobenzaldehyde, we have considered up to three different orientations of the 4-nitrobenzaldehyde on Ni-Mo_2C (Fig. S9 in the ESM), namely the NO_2-vertex mode, the CHO-vertex mode, and the flat-laying mode (M-π), respectively. The examination showed that the NO_2-vertex mode is the most stable with the lowest energy, which is in line with the excellent chemoselectivity toward the $-NO_2$ hydrogenation (Table 1). Further, we investigated the H_2 adsorption behavior and found that H_2 is only physisorbed on pure Mo_2C (adsorption energy near zero), while chemisorption occurs on Ni-Mo_2C with an adsorption energy as large as 0.7 eV. Hence, it is likely that the physisorbed molecular hydrogen species on Mo_2C spill over to the surface of the metallic Ni particles where they are dissociated and activated, as corroborated by the Mo K-edge XANES spectra, cf. Fig. 3(e). The dissociation barrier of H_2 is reduced from ~ 0.2 to ~ 0.1 eV when a Ni particle is present. The activating adsorption of both 4-nitrobenzaldehyde and H_2 can be attributed to the positively charged Ni particles, which facilitate the electron transfer between the reactants and the catalyst.

Based on the experimental and DFT results, a tentative pathway of the hydrogenation over Ni-MoC_x catalyst is proposed schematically in Fig. 7. Due to the stronger electron absorption ability of the nitrile group compared to the formyl group, nitrile should be preferentially absorbed on the surface of positively charged Ni particles. Dihydrogen is prone to be adsorbed on the MoC_x surface and to spill over to the metallic nickel particles, where it dissociates to [H] and reacts with the nitro group of chemisorbed nitrobenzaldehyde, forming aminobenzaldehyde. Finally, the product easily desorbs from the catalyst surface due to the electron donation character of the amino group.

4 Conclusions

An efficient Ni-MoC_x nanocomposite catalyst has been prepared via simple carburization of $(NH_4)_4Ni(OH)_6Mo_6O_{18}$ clusters. In this catalyst, the Ni particles of ~ 45 nm size interact strongly with the MoC_x support, as evidenced by XPS, XAS, and DFT calculations. The Ni-MoC_x nanocomposite exhibits high activity and chemoselectivity in the catalytic reduction of nitroaromatics to corresponding amines, whereas it shows virtually inertness for the reduction of other unsaturated aryl substituents such as vinyl, formyl, halides, and cyano groups even at long reaction time. This behavior is attributed to a strong synergistic effect caused by electron transfer from the metallic Ni particles to the MoC_x support as substantiated by XPS, XAS, and DFT. Hydrogen–deuterium exchange experiments indicate that the Ni-MoC_x has a strong ability for dissociating hydrogen molecules at relatively low temperatures (> 50 °C). *In-situ* Mo K-edge XANES spectra as well as DFT unravel that molecular hydrogen is physisorbed on the Mo_2C support and likely spills over to the metallic Ni particles where it is dissociated and selectively reacts with nitro groups. All these findings may pave the way to the design of other low-cost efficient non-noble metal catalysts for the chemoselective hydrogenation of fine chemicals.

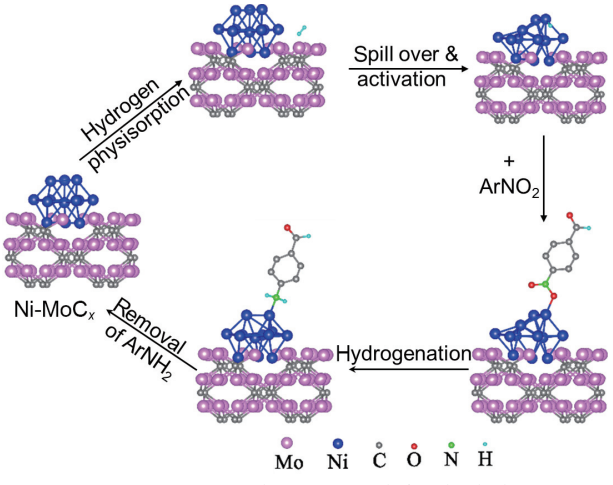

Figure 7 Tentative reaction pathway proposed for the hydrogenation of nitrobenzaldehyde over Ni-MoC_x.

Acknowledgements

We thank the National Natural Science Foundation of China for supporting this work (No. 22172167). The 1W1B beamline of Beijing Synchrotron Radiation Facility and BL14W1 beamline of Shanghai Synchrotron Radiation Facility are acknowledged for providing the beam time.

Funding note: Open Access funding provided by Swiss Federal Institute of Technology Zurich.

Electronic Supplementary Material: Supplementary material (histogram of Ni particle size, Ni K-edge EXAFS, recyclability test, comparison of TOFs of various catalysts, and DFT analyses of substrate adsorption) is available in the online version of this article at https://doi.org/10.1007/s12274-023-5598-x.

References

[1] Song, J. J.; Huang, Z. F.; Pan, L.; Li, K.; Zhang, X. W.; Wang, L.; Zou, J. J. Review on selective hydrogenation of nitroarene by catalytic, photocatalytic and electrocatalytic reactions. *Appl. Catal. B:Environ.* **2018**, *227*, 386–408.

[2] Formenti, D.; Ferretti, F.; Scharnagl, F. K.; Beller, M. Reduction of nitro compounds using 3d-non-noble metal catalysts. *Chem. Rev.* **2019**, *119*, 2611–2680.

[3] Ono, N. *The Nitro Group in Organic Synthesis*; Wiley-VCH: New York, 2001.

[4] Jin, R. C.; Li, G.; Sharma, S.; Li, Y. W.; Du, X. S. Toward active-site tailoring in heterogeneous catalysis by atomically precise metal nanoclusters with crystallographic structures. *Chem. Rev.* **2021**, *121*, 567–648.

[5] Li, R. Z.; Wang, D. S. Understanding the structure–performance relationship of active sites at atomic scale. *Nano Res.* **2022**, *15*, 6888–6923.

[6] Li, Z. J.; Leng, L. P.; Lu, X. W.; Zhang, M. Y.; Xu, Q.; Horton, J.

H.; Zhu, J. F. Single palladium atoms stabilized by β-FeOOH nanorod with superior performance for selective hydrogenation of cinnamaldehyde. *Nano Res.* **2022**, *15*, 3114–3121.

[7] Wang, J. S.; Du, C.; Wei, Q. H.; Shen, W. Z. Two-dimensional Pd nanosheets with enhanced catalytic activity for selective hydrogenation of nitrobenzene to aniline. *Energy Fuels* **2021**, *35*, 4358–4366.

[8] Harraz, F. A.; El-Hout, S. E.; Killa, H. M.; Ibrahim, I. A. Palladium nanoparticles stabilized by polyethylene glycol: Efficient, recyclable catalyst for hydrogenation of styrene and nitrobenzene. *J. Catal.* **2012**, *286*, 184–192.

[9] Wang, X. Y.; Huang, C. R.; Li, X. H.; Xie, C. X.; Yu, S. T. PVA-encapsulated palladium nanoparticles: Eco-friendly and highly selective catalyst for hydrogenation of nitrobenzene in aqueous medium. *Chem. Asian J.* **2019**, *14*, 2266–2272.

[10] Li, Y. H.; Zhu, L. H.; Yan, K. Q.; Zheng, J. B.; Chen, B. H.; Wang, W. J. A novel modification method for nickel foam support and synthesis of a metal-supported hierarchical monolithic Ni@Pd catalyst for benzene hydrogenation. *Chem. Eng. J.* **2013**, *226*, 166–170.

[11] Serna, P.; Corma, A. Transforming nano metal nonselective particulates into chemoselective catalysts for hydrogenation of substituted nitrobenzenes. *ACS Catal.* **2015**, *5*, 7114–7121.

[12] Qin, Z. X.; Hu, S.; Han, W. H.; Li, Z. W.; Xu, W. W.; Zhang, J. J.; Li, G. Tailoring optical and photocatalytic properties by single-Ag-atom exchange in $Au_{13}Ag_{12}(PPh_3)_{10}Cl_8$ nanoclusters. *Nano Res.* **2022**, *15*, 2971–2976.

[13] Shi, Q. Q.; Zhang, X. Y.; Liu, X.; Xu, L. L.; Liu, B. C.; Zhang, J.; Xu, H.; Han, Z. K.; Li, G. *In-situ* exfoliation and assembly of 2D/2D g-C_3N_4/TiO_2(B) hierarchical microflower: Enhanced photo-oxidation of benzyl alcohol under visible light. *Carbon* **2022**, *196*, 401–409.

[14] Blaser, H. U.; Steiner, H.; Studer, M. Selective catalytic hydrogenation of functionalized nitroarenes: An update. *ChemCatChem* **2009**, *1*, 210–221.

[15] Torres, G. C.; Jablonski, E. L.; Baronetti, G. T.; Castro, A. A.; de Miguel, S. R.; Scelza, O. A.; Blanco, M. D.; Pen˜a Jiménez, M. A.; Fierro, J. L. G. Effect of the carbon pre-treatment on the properties and performance for nitrobenzene hydrogenation of Pt/C catalysts. *Appl. Catal. A Gen.* **1997**, *161*, 213–226.

[16] Nie, R. F.; Wang, J. H.; Wang, L. N.; Qin, Y.; Chen, P.; Hou, Z. Y. Platinum supported on reduced graphene oxide as a catalyst for hydrogenation of nitroarenes. *Carbon* **2012**, *50*, 586–596.

[17] Huang, X. Q.; Li, Y. J.; Li, Y. J.; Zhou, H. L.; Duan, X. F.; Huang, Y. Synthesis of PtPd bimetal nanocrystals with controllable shape, composition, and their tunable catalytic properties. *Nano Lett.* **2012**, *12*, 4265–4270.

[18] Shi, Q. Q.; Qin, Z. X.; Sharma, S.; Li, G. Recent progress in heterogeneous catalysis by atomically and structurally precise metal nanoclusters. *Chem. Rec.* **2021**, *21*, 879–892.

[19] Shi, Q. Q.; Qin, Z. X.; Yu, C. L.; Waheed, A.; Xu, H.; Gao, Y.; Abroshan, H.; Li, G. Experimental and mechanistic understanding of photo-oxidation of methanol catalyzed by CuO/TiO_2-spindle nanocomposite: Oxygen vacancy engineering. *Nano Res.* **2020**, *13*, 939–946.

[20] Zhang, Y. F.; Yang, X. J.; Zhou, Y.; Li, G.; Li, Z. M.; Liu, C.; Bao, M.; Shen, W. J. Selective hydrogenation of the C=C bond in α,β-unsaturated aldehydes and ketones over ultra-small Pd-Au clusters. *Nanoscale* **2016**, *8*, 18626–18629.

[21] Ryabchuk, P.; Agostini, G.; Pohl, M. M.; Lund, H.; Agapova, A.; Junge, H.; Junge, K.; Beller, M. Intermetallic nickel silicide nanocatalyst—A non-noble metal-based general hydrogenation catalyst. *Sci. Adv.* **2018**, *4*, eaat0761.

[22] Pisiewicz, S.; Formenti, D.; Surkus, A. E.; Pohl, M. M.; Radnik, J.; Junge, K.; Topf, C.; Bachmann, S.; Scalone, M.; Beller, M. Synthesis of nickel nanoparticles with N-doped graphene shells for catalytic reduction reactions. *ChemCatChem* **2016**, *8*, 129–134.

[23] Hahn, G.; Ewert, J. K.; Denner, C.; Tilgner, D.; Kempe, R. A reusable mesoporous nickel nanocomposite catalyst for the selective hydrogenation of nitroarenes in the presence of sensitive functional groups. *ChemCatChem* **2016**, *8*, 2461–2465.

[24] Miyazaki, M.; Ariyama, K.; Furukawa, S.; Takayama, T.; Komatsu, T. Chemoselective hydrogenation of nitroarenes using Ni-Fe alloy catalysts at ambient pressure. *ChemistrySelect* **2021**, *6*, 5538–5544.

[25] Tian, S. B.; Hu, M.; Xu, Q.; Gong, W. B.; Chen, W. X.; Yang, J. R.; Zhu, Y. Q.; Chen, C.; He, J.; Liu, Q. et al. Single-atom Fe with Fe_1N_3 structure showing superior performances for both hydrogenation and transfer hydrogenation of nitrobenzene. *Sci. China Mater.* **2021**, *64*, 642–650.

[26] Cui, X. L.; Zhou, X.; Dong, Z. P. Ultrathin γ-Fe_2O_3 nanosheets as a highly efficient catalyst for the chemoselective hydrogenation of nitroaromatic compounds. *Catal. Commun.* **2018**, *107*, 57–61.

[27] Yun, R. R.; Zhan, F. Y.; Li, N.; Zhang, B. B.; Ma, W. J.; Hong, L. R.; Sheng, T.; Du, L. T.; Zheng, B. S.; Liu, S. J. Fe single atoms and Fe_2O_3 clusters liberated from N-doped polyhedral carbon for chemoselective hydrogenation under mild conditions. *ACS Appl. Mater. Interfaces* **2020**, *12*, 34122–34129.

[28] Hu, A.; Lu, X. H.; Cai, D. M.; Pan, H. J.; Jing, R.; Xia, Q. H.; Zhou, D.; Xia, Y. D. Selective hydrogenation of nitroarenes over MOF-derived Co@CN catalysts at mild conditions. *Mol. Catal.* **2019**, *472*, 27–36.

[29] Sun, X. H.; Olivos-Suarez, A. I.; Osadchii, D.; Romero, M. J. V.; Kapteijn, F.; Gascon, J. Single cobalt sites in mesoporous N-doped carbon matrix for selective catalytic hydrogenation of nitroarenes. *J. Catal.* **2018**, *357*, 20–28.

[30] Liu, W. J.; Tian, K.; Jiang, H. One-pot synthesis of Ni-$NiFe_2O_4$/carbon nanofiber composites from biomass for selective hydrogenation of aromatic nitro compounds. *Green Chem.* **2015**, *17*, 821–826.

[31] Xia, J. W.; He, G. Y.; Zhang, L. L.; Sun, X. Q.; Wang, X. Hydrogenation of nitrophenols catalyzed by carbon black-supported nickel nanoparticles under mild conditions. *Appl. Catal. B:Environ.* **2016**, *180*, 408–415.

[32] Sheng, Y.; Lin, X. R.; Yue, S. N.; Liu, Y.; Zou, X. J.; Wang, X. G.; Lu, X. G. Highly efficient non-noble metallic NiCu nanoalloy catalysts for hydrogenation of nitroarenes. *Mater. Adv.* **2021**, *2*, 6722–6730.

[33] Ye, T. N.; Lu, Y. F.; Li, J.; Nakao, T.; Yang, H. S.; Tada, T.; Kitano, M.; Hosono, H. Copper-based intermetallic electride catalyst for chemoselective hydrogenation reactions. *J. Am. Chem. Soc.* **2017**, *139*, 17089–17097.

[34] Wolfbeisser, A.; Sophiphun, O.; Bernardi, J.; Wittayakun, J.; Föttinger, K.; Rupprechter, G. Methane dry reforming over ceria-zirconia supported Ni catalysts. *Catal. Today* **2016**, *277*, 234–245.

[35] Wei, X. J.; Rang, X.; Zhu, W. H.; Xiang, M.; Deng, Y. Y.; Jiang, F. H.; Mao, R.; Zhang, Z. W.; Kong, X. Q.; Wang, F. Morphology effect of CeO_2 on Ni/CeO_2 catalysts for selective hydrogenation of cinnamaldehyde. *Chem. Phys.* **2021**, *542*, 111079.

[36] Meng, X. C.; Cheng, H. Y.; Akiyama, Y.; Hao, Y. F.; Qiao, W. B.; Yu, Y. C.; Zhao, F. Y.; Fujita, S. I.; Arai, M. Selective hydrogenation of nitrobenzene to aniline in dense phase carbon dioxide over Ni/γ-Al_2O_3: Significance of molecular interactions. *J. Catal.* **2009**, *264*, 1–10.

[37] Millán, R.; Soriano, M. D.; Moreno, C. C.; Boronat, M.; Concepción, P. Combined spectroscopic and computational study of nitrobenzene activation on non-noble metals-based mono- and bimetallic catalysts. *Nanomaterials* **2021**, *11*, 2037.

[38] Beswick, O.; Lamey, D.; Muriset, F.; LaGrange, T.; Oberson, L.; Yoon, S.; Sulman, E.; Dyson, P. J.; Kiwi-Minsker, L. Ni-based structured catalyst for selective 3-phase hydrogenation of nitroaromatics. *Catal. Today* **2016**, *273*, 244–251.

[39] Sun, Y. Y.; Li, X. W.; Cai, Z. S.; Bai, H. Z.; Tang, G. P.; Hou, Z. Y. Synthesis of 3D N-doped graphene/carbon nanotube hybrids with encapsulated Ni NPs and their catalytic application in the hydrogenation of nitroarenes. *Catal. Sci. Technol.* **2018**, *8*, 4858–4863.

[40] Wang, F.; Li, T.; Shi, Y.; Jiao, H. J. Molybdenum carbide supported metal catalysts (M_n/Mo_xC; M = Co, Ni, Cu, Pd, Pt)—Metal and surface dependent structure and stability. *Catal. Sci. Technol.* **2020**, *10*, 3029–3046.

[41] Dong, J. H.; Fu, Q.; Jiang, Z.; Mei, B. B.; Bao, X. H. Carbide-supported Au catalysts for water–gas shift reactions: A new territory for the strong metal–support interaction effect. *J. Am. Chem. Soc.* **2018**, *140*, 13808–13816.
[42] Lin, L. L.; Zhou, W.; Gao, R.; Yao, S. Y.; Zhang, X.; Xu, W. Q.; Zheng, S. J.; Jiang, Z.; Yu, Q. L.; Li, Y. W. et al. Low-temperature hydrogen production from water and methanol using Pt/α-MoC catalysts. *Nature* **2017**, *544*, 80–83.
[43] Zhang, J. W.; Huang, Y. C.; Li, G.; Wei. Y. G. Recent advances in alkoxylation chemistry of polyoxometalates: From synthetic strategies, structural overviews to functional applications. *Coord. Chem. Rev.* **2019**, *378*, 395–414.
[44] Wen, Z. Y.; Li, Z. M.; Ge, Q. J.; Zhou, Y.; Sun, J.; Abroshan, H.; Li, G. Robust nickel cluster@Mes-HZSM-5 composite nanostructure with enhanced catalytic activity in the DTG reaction. *J. Catal.* **2018**, *363*, 26–33.
[45] Grimme, S. Semiempirical GGA-type density functional constructed with a long-range dispersion correction. *J. Comput. Chem.* **2006**, *27*, 1787–1799.
[46] Kresse, G.; Furthmüller, J. Efficient iterative schemes for *ab initio* total-energy calculations using a plane-wave basis set. *Phys. Rev. B* **1996**, *54*, 11169–11186.
[47] Perdew, J. P.; Burke, K.; Ernzerhof, M. Generalized gradient approximation made simple. *Phys. Rev. Lett.* **1996**, *77*, 3865–3868.
[48] Perdew, J. P.; Wang, Y. Pair-distribution function and its coupling-constant average for the spin-polarized electron gas. *Phys. Rev. B* **1992**, *46*, 12947–12954.
[49] Blöchl, P. E. Projector augmented-wave method. *Phys. Rev. B* **1994**, *50*, 17953–17979.
[50] Chadi, D. J. Special points for Brillouin-zone integrations. *Phys. Rev. B* **1977**, *16*, 1746–1747.
[51] Lin, H. L.; Shi, Z. P.; He, S. N.; Yu, X.; Wang, S. N.; Gao, Q. S.; Tang, Y. Heteronanowires of MoC-Mo_2C as efficient electrocatalysts for hydrogen evolution reaction. *Chem. Sci.* **2016**, *7*, 3399–3405.
[52] Shi, Z. P.; Wang, Y. X.; Lin, H. L.; Zhang, H. B.; Shen, M. K.; Xie, S. H.; Zhang, Y. H.; Gao, Q. S.; Tang, Y. Porous nanoMoC@graphite shell derived from a MOFs-directed strategy: An efficient electrocatalyst for the hydrogen evolution reaction. *J. Mater. Chem. A* **2016**, *4*, 6006–6013.
[53] Li, M. X.; Zhu, Y.; Wang, H. Y.; Wang, C.; Pinna, N.; Lu, X. F. Ni strongly coupled with Mo_2C encapsulated in nitrogen-doped carbon nanofibers as robust bifunctional catalyst for overall water splitting. *Adv. Energy Mater.* **2019**, *9*, 1803185.
[54] Mansour, A. N.; Melendres, C. A. Characterization of slightly hydrated $Ni(OH)_2$ by XPS. *Surf. Sci. Spectra* **1994**, *3*, 247–254.
[55] Fang, Q. H.; Qin, Z. X.; Shi, Y. T.; Liu, F.; Barkaoui, S.; Abroshan, H.; Li, G. Au/NiO composite: A catalyst for one-pot cascade conversion of furfural. *ACS Appl. Energy Mater.* **2019**, *2*, 2654–2661.
[56] Wang, T.; Dong, Z.; Fu, T.; Zhao, Y. C.; Wang, T.; Wang, Y. Z.; Chen, Y.; Han, B. H.; Ding, W. P. Nickel embedded in N-doped porous carbon for the hydrogenation of nitrobenzene to p-aminophenol in sulphuric acid. *Chem. Commun.* **2015**, *51*, 17712–17715.
[57] Jiang, C. J.; Shang, Z. Y.; Liang, X. H. Chemoselective transfer hydrogenation of nitroarenes catalyzed by highly dispersed, supported nickel nanoparticles. *ACS Catal.* **2015**, *5*, 4814–4818.
[58] Kim, M.; Kim, S.; Song, D.; Oh, S.; Chang, K. J.; Cho, E. Promotion of electrochemical oxygen evolution reaction by chemical coupling of cobalt to molybdenum carbide. *Appl. Catal. B:Environ.* **2018**, *227*, 340–348.
[59] Cao, Y. H.; Guo, S.; Yu, C. L.; Zhang, J. W.; Pan, X. L.; Li, G. Ionic liquid-assisted one-step preparation of ultrafine amorphous metallic hydroxide nanoparticles for the highly efficient oxygen evolution reaction. *J. Mater. Chem. A* **2020**, *8*, 15767–15773.
[60] Mao, J. J.; Chen, W. X.; He, D. S.; Wan, J. W.; Pei, J. J.; Dong, J. C.; Wang, Y.; An, P. F.; Jin, Z.; Xing, W. et al. Design of ultrathin Pt-Mo-Ni nanowire catalysts for ethanol electrooxidation. *Sci. Adv.* **2017**, *3*, e1603068.
[61] Cao, Y. H.; Su, Y.; Xu, L. L.; Yang, X. H.; Han, Z. K.; Cao, R.; Li, G. Oxygen vacancy-rich amorphous FeNi hydroxide nanoclusters as an efficient electrocatalyst for water oxidation. *J. Energy Chem.* **2022**, *71*, 167–173.
[62] Wojcieszak, R.; Monteverdi, S.; Ghanbaja, J.; Bettahar, M. M. Study of Ni-Ag/SiO_2 catalysts prepared by reduction in aqueous hydrazine. *J. Colloid Interface Sci.* **2008**, *317*, 166–174.
[63] Liu, C.; Abroshan, H.; Yan, C. Y.; Li, G.; Haruta, M. One-pot synthesis of $Au_{11}(PPh_2Py)_7Br_3$ for the highly chemoselective hydrogenation of nitrobenzaldehyde. *ACS Catal.* **2016**, *6*, 92–99.
[64] Tan, Y.; Liu, X. Y.; Li, L.; Kang, L. L.; Wang, A. Q.; Zhang, T. Effects of divalent metal ions of hydrotalcites on catalytic behavior of supported gold nanocatalysts for chemoselective hydrogenation of 3-nitrostyrene. *J. Catal.* **2018**, *364*, 174–182.
[65] Ito, S.; Wang, X. W.; Waheed, A.; Li, G.; Maeda, N.; Meier, D. M.; Naito, S.; Baiker, A. Support effects in iridium-catalyzed aerobic oxidation of benzyl alcohol studied by modulation-excitation attenuated total reflection IR spectroscopy. *J. Catal.* **2021**, *393*, 42–50.